Can magnetic fabrics distinguish between aseismic and seismic slip along faults?

Ran Issachar[1], Tsafrir Levi[1], and Ram Weinberger[1]

[1]Geological Survey of Israel

November 21, 2022

Abstract

A long-standing problem in paleoseismic studies is to distinguish between aseismic and seismic slips along faults. We address this problem by characterizing the magnetic fabrics of rock samples around mesoscale normal faults of aseismic origin, and comparing them to those around co-seismic normal faults. Detailed sampling profiles along traverses, <0.2 m up to ~20 m from both sides of the faults, indicate symmetric and unchangeable magnetic fabrics of deformation origin that are coaxial with the regional strain field. These results are essentially different from magnetic fabrics detected around co-seismic normal faults, which show fault-related fabrics with asymmetric and changeable orientations. The analysis demonstrates two end-member cases of magnetic fabrics in association with aseismic and seismic slips along faults. We suggest that magnetic fabric analysis provides a powerful and efficient tool to characterize inelastic deformation around faults, enabling to distinguish between seismic and aseismic slip histories.

@AGU PUBLICATIONS
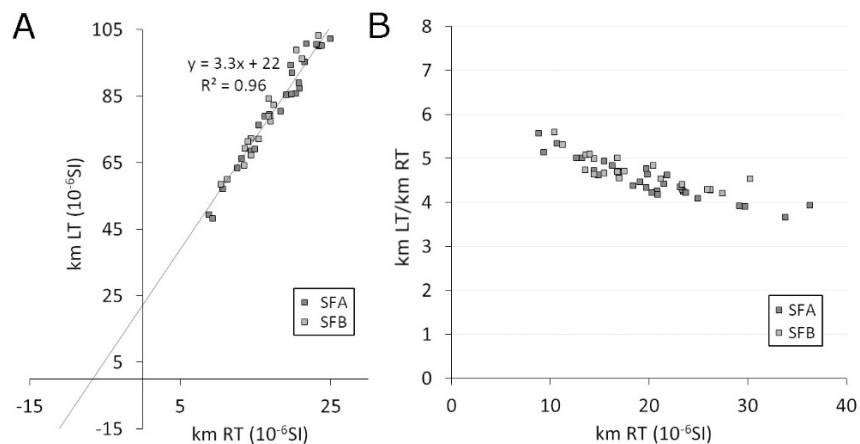
Geophysical Research Letters

Figure S1. Room-temperature mean susceptibility (k_m^{RT}) and low-temperature mean susceptibility (k_m^{LT}) of chalk samples, indicating that paramagnetic and diamagnetic minerals are the main contributors to the rock mean susceptibility (see Issachar et al., 2018 for details). (A) k_m^{LT} versus k_m^{RT} plot showing a linear correlation with a slop of 3.3. (B) k_m^{LT}/k_m^{RT} versus k_m^{RT} plot showing an average amplification factor of 4.6 ± 0.4.
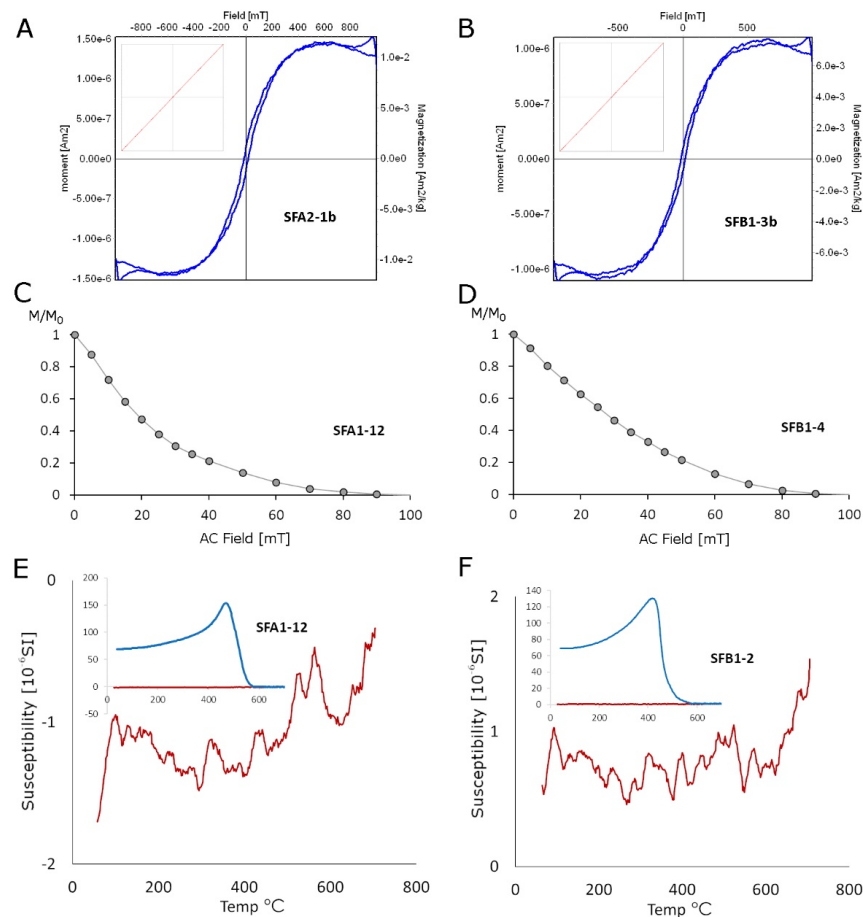

2

Figure S2. Magnetic mineralogy tests for representing samples. (A) and (B) Vibrating Sample Magnetometer (VSM) hysteresis loops. The raw data (red curves in the small boxes) indicates the dominancy of paramagnetic minerals (positive slope) and negligible contribution of ferromagnetic minerals (linear slop). The slope-corrected data (blue curves) indicates the presence of low-coercivity ferromagnetic minerals. (C) and (D) Alternating Field demagnetization curves (AF curves). The samples were first magnetized by AC field of 100 mT and DC field of 500 ?T and then demagnetized in 5 mT steps. The curves indicate that most of the magnetic remanence (up to 90%) is lost by a demagnetization field of 60 mT, suggesting that mostly low-coercivity minerals carry the remanent magnetization. (E) and (F) Temperature-dependent susceptibility curves (k(T)). The susceptibility changes during heating (red curves) indicate slight variations, suggesting negligible contribution of ferromagnetic minerals. The cooling curves (blue) indicate substantial susceptibility increase at ˜580 °C, suggesting the formation of magnetite.

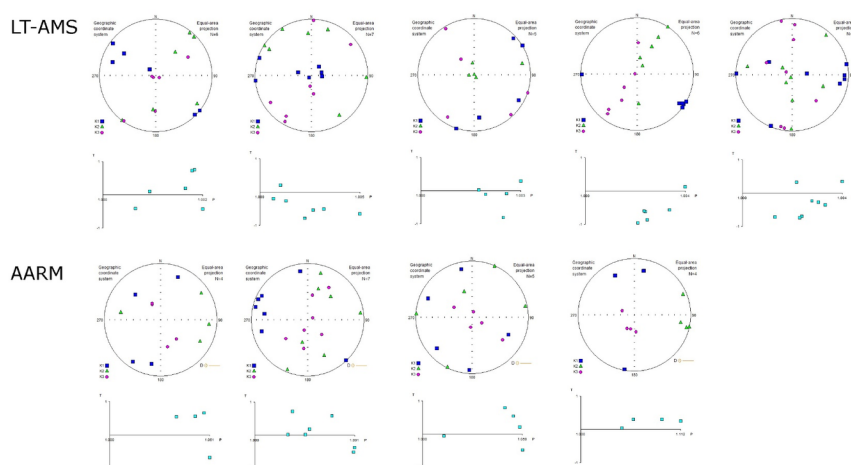**Figure S3.** Fault A - LT-AMS and AARM magnetic fabrics. Stereoplots are lower-hemisphere, equal-area projection of principal axes.
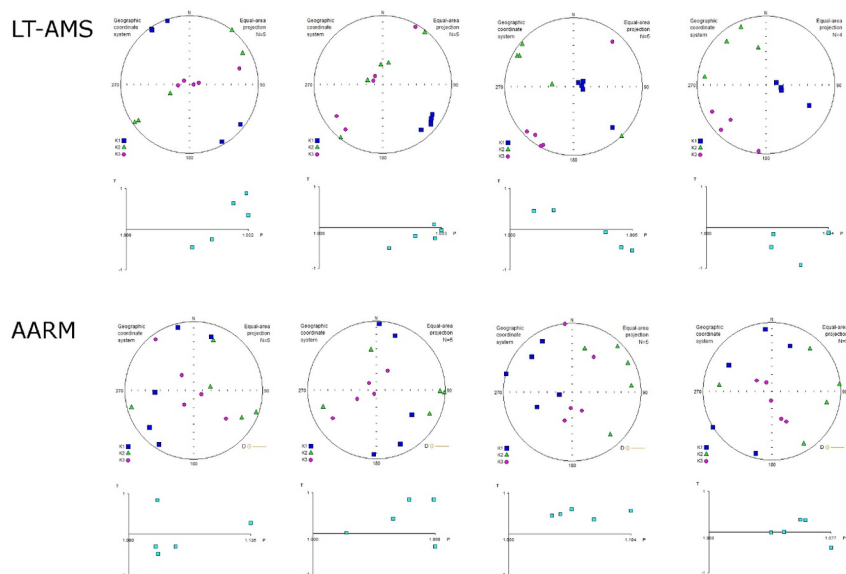

3

Figure S4. Fault B - LT-AMS and AARM magnetic fabrics. Stereoplots are lower-hemisphere, equal-area projection of principal axes.
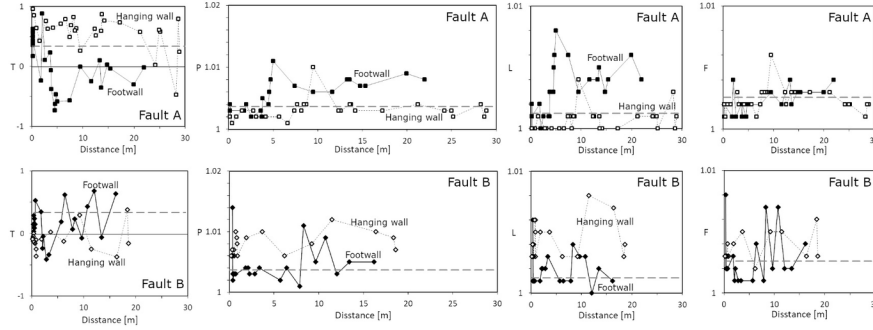

Figure S5. RT-AMS parameters shape of anisotropy (T), degree of anisotropy (P) magnetic lineation (L) and magnetic foliation (F) versus distance from footwall samples (black symbols) and hanging wall samples (empty symbols). Dashed lines represent the average values of the reference samples.

Table S1. Sampling and RT-AMS data including the distance of the sample from fault plane, mean susceptibility (km), shape of anisotropy (T), degree of anisotropy (P) magnetic lineation (L) and magnetic foliation (F). The coordinates of the faults are: Fault A (31.128362, 34.764077); Fault B (31.127435, 34.763659).

Fault	Block	Distance from fault plane (m)	km ($\times 10^{-6}$ SI)	P	T	L	F
Fault A	Hanging wall	28.9	18.1	1.003	0.243	1.008	1.005
		28.7	27.5	1.002	0.792	1.003	1.005
		28.3	16.4	1.004	-0.469	1.003	1.002
		25.2	20.2	1.002	0.581	1.005	1.005
		25.0	17.1	1.003	0.610	1.005	1.004
		24.2	13.9	1.003	0.027	1.003	1.003
		21.2	16.2	1.004	0.577	1.005	1.003
		17.3	17.7	1.003	0.734	1.006	1.003
		14.2	12.0	1.003	0.762	1.006	1.004
		13.7	9.9	1.004	0.869	1.003	1.003
		13.6	9.0	1.004	0.592	1.004	1.003
		12.6	12.6	1.003	0.515	1.003	1.003
		12.4	13.4	1.003	0.625	1.003	1.003
		9.5	6.0	1.01	0.261	1.004	1.003
		8.7	11.7	1.004	0.632	1.003	1.003
		8.5	10.8	1.004	0.599	1.003	1.003
		8.2	11.3	1.003	0.820	1.006	1.008
		7.7	12.6	1.004	0.688	1.001	1.002
		7.4	10.2	1.003	0.494	1.001	1.002
		6.6	24.4	1.001	0.786	1.001	1.002
		5.7	16.0	1.002	0.711	1.001	1.002
		4.2	16.8	1.002	0.643	1.001	1.002
		3.1	15.5	1.002	0.630	1.001	1.002

4

Fault	Block	Distance from fault plane (m)	km (×10^{-6} SI)	P	T	L	F
		2.8	14.5	1.003	0.759	1.001	1.002
		1.5	19.1	1.003	0.424	1.001	1.002
		0.9	23.5	1.002	0.641	1.001	1.003
		0.4	29.8	1.001	0.852	1.002	1.001
		0.2	36.3	1.002	0.956	1.002	1.002
	Footwall	<0.2	14.6	1.003	0.504	1.002	1.001
		<0.2	33.9	1.002	0.418	1.003	1.001
		<0.2	29.2	1.002	0.627	1.001	1.001
		<0.2	20.8	1.002	0.359	1.001	1.004
		<0.2	14.9	1.004	0.171	1.001	1.001
		<0.2	15.8	1.002	0.437	1.004	1.007
		<0.2	21.5	1.002	0.355	1.003	1.002
		<0.2	18.4	1.003	0.566	1.003	1.007
		<0.2	12.6	1.003	0.415	1.000	1.002
		<0.2	8.9	1.003	0.420	1.002	1.002
		1.8	10.7	1.003	-0.233	1.001	1.004
		2.0	16.9	1.004	0.882	1.003	1.002
		2.6	26.2	1.002	0.105	1.002	1.001
		3.6	21.8	1.003	0.230	1.002	1.003
		3.7	19.9	1.002	-0.062	1.001	1.003
		3.8	20.9	1.005	-0.376	1.001	1.001
		4.5	24.9	1.004	-0.729	1.002	1.001
		4.6	23.4	1.006	-0.626	1.001	1.004
		4.7	13.2	1.008	-0.463	1.001	1.003
		5.0	9.4	1.011	-0.582	1.001	1.003
		7.4	16.9	1.007	-0.565	1.000	1.003
		9.5	23.8	1.006	-0.004	1.001	1.004
		11.7	20.4	1.006	-0.246	1.000	1.003
		13.3	21.5	1.008	0.100	1.008	1.005
		13.6	19.8	1.008	-0.351	1.003	1.005
		14.8	23.2	1.007	0.032	1.003	1.002
		15.4	21.2	1.007	-0.033	1.005	1.005
		20.0	16.3	1.009	-0.302	1.005	1.004
		22.0	19.8	1.008	-0.015	1.003	1.003
Fault B	Hanging wall	18.6	26.3	1.007	-0.157	1.004	1.003
		18.4	20.4	1.009	0.383	1.003	1.006
		16.4	27.5	1.010	-0.370	1.007	1.003
		11.5	16.8	1.012	-0.247	1.008	1.005
		9.2	16.6	1.008	0.298	1.003	1.005
		6.2	30.3	1.006	-0.124	1.003	1.002
		3.7	18.3	1.010	0.026	1.005	1.005
		1.9	17.4	1.009	-0.087	1.005	1.004
		0.9	21.3	1.006	-0.098	1.003	1.003
		0.9	18.9	1.008	-0.358	1.005	1.003
		0.8	17.5	1.009	-0.246	1.006	1.003
		0.7	14.5	1.010	-0.157	1.006	1.004
		0.5	24.6	1.006	-0.145	1.003	1.003

Fault	Block	Distance from fault plane (m)	km (×10⁻⁶ SI)	P	T	L	F
		0.5	21.2	1.007	-0.123	1.004	1.003
		0.4	26.0	1.006	0.001	1.003	1.003
		0.3	23.3	1.006	-0.042	1.003	1.003
		0.3	23.4	1.007	-0.123	1.004	1.003
		0.2	25.9	1.006	-0.074	1.003	1.003
		0.2	25.7	1.006	-0.090	1.003	1.003
	Footwall	0.3	3.8	1.014	0.150	1.006	1.008
		0.4	14.5	1.003	0.034	1.001	1.002
		0.4	15.5	1.002	0.290	1.001	1.002
		0.5	13.6	1.003	0.097	1.001	1.002
		0.5	13.7	1.003	0.239	1.001	1.002
		0.5	14.5	1.003	0.084	1.001	1.002
		0.5	16.3	1.003	0.241	1.001	1.002
		0.7	17.0	1.003	0.148	1.001	1.002
		0.7	16.8	1.003	0.529	1.001	1.002
		1.8	13.6	1.004	0.349	1.001	1.003
		2.1	10.4	1.004	-0.234	1.002	1.001
		2.2	11.3	1.003	-0.043	1.002	1.002
		2.8	14.0	1.003	-0.409	1.002	1.001
		3.3	12.2	1.004	-0.338	1.003	1.001
		5.7	14.8	1.002	0.190	1.001	1.001
		6.4	4.2	1.004	0.621	1.001	1.004
		7.9	26.7	1.001	0.069	1.001	1.001
		8.3	6.0	1.011	0.234	1.004	1.007
		9.7	17.7	1.005	-0.074	1.003	1.002
		10.8	8.8	1.009	0.434	1.003	1.007
		12.0	28.6	1.003	0.683	1.000	1.002
		13.4	32.3	1.005	-0.058	1.002	1.002
		16.2	10.0	1.005	-0.157	1.001	1.004
Reference samples	Reference samples	>50	13.3	1.005	0.551	1.001	1.004
		>50	15.3	1.004	0.488	1.001	1.003
		>50	25.7	1.004	0.657	1.001	1.003
		>50	35.1	1.003	0.766	1.000	1.003
		>50	18.0	1.005	0.529	1.001	1.004

6

Can magnetic fabrics distinguish between aseismic and seismic slip along faults?

R. Issachar[1], T. Levi[1] and R. Weinberger[1,2]

[1]Geological Survey of Israel, Jerusalem, Israel

[2]Department of Geological and Environmental Sciences, Ben Gurion University of the Negev, Beer Sheva, Israel

Key Points

(1) Magnetic fabrics are analyzed near faults in order to distinguish between aseismic and seismic slips.

(2) Analysis demonstrates two end-member types of magnetic fabrics - symmetric and unchangeable vs. asymmetric and changeable.

(3) Magnetic fabrics near aseismic and seismic faults are different and enable to distinguish between slip histories.

Abstract

A long-standing problem in paleoseismic studies is to distinguish between aseismic and seismic slips along faults. We address this problem by characterizing the magnetic fabrics of rock samples around mesoscale normal faults of aseismic origin, and comparing them to those around co-seismic normal faults. Detailed sampling profiles along traverses, <0.2 m up to ~20 m from both sides of the faults, indicate symmetric and unchangeable magnetic fabrics of deformation origin that are coaxial with the regional strain field. These results are essentially different from magnetic fabrics detected around co-seismic normal faults, which show fault-related fabrics with asymmetric and changeable orientations. The analysis demonstrates two end-member cases of

1

23 magnetic fabrics in association with aseismic and seismic slips along faults. We suggest that

24 magnetic fabric analysis provides a powerful and efficient tool to characterize inelastic

25 deformation around faults, enabling to distinguish between seismic and aseismic slip histories.

26 **Plain Language Summary**

27 A long-standing problem in the study of Earth's deformation is to differentiate between faults

28 that originate during earthquake evens (seismic faults) and those that are creeping due to long-

29 lasting, regional stresses (aseismic faults). We address this problem by characterizing the

30 magnetic fabrics of rock samples around faults of aseismic origin and compare them with

31 magnetic fabrics around faults of seismic origin. The magnetic fabrics mimics the distribution of

32 minerals and grains in the rocks, and, hence, are commonly served as a tool to detect "order" and

33 "disorder" in rocks. The results indicate that around the aseismic faults the magnetic fabrics are

34 uniform and reflect the large-scale regional deformation, whereas around the seismic faults the

35 magnetic fabrics are changeable and reflect the local deformation along the faults. Since all the

36 faults were formed under similar sedimentary conditions, we demonstrate two end-member cases

37 of magnetic fabrics in association with aseismic and seismic slips along faults. We suggest that

38 magnetic fabric analysis provides a powerful and efficient tool to characterize inelastic

39 deformation around faults, enabling us to distinguish between seismic and aseismic slip histories.

2

1. Introduction

Faults are common geological features reflecting deep and shallow crustal processes and, as such, are used to decipher different geological environments. Faults accumulate displacement by slow aseismic slip (creep) at plate tectonic rates (10^{-12} to 10^{-10} m/s) or by fast seismic slip of earthquake rates (10^{-4} to 10 m/s). There are several suggested criteria to recognize seismic slip along faults, including pseudotachylytes that form during frictional heating, pulverized rocks that form by transient stresses at the rupture tip (Rowe and Griffith, 2015), and fault-related texture of hematite (Ault, 2020). Nevertheless, seismic slip does not necessarily leave distinct petrological traces in the host rock, especially in cases where the rupture reaches close to the surface. The characteristics of host-rock deformation around faults have the potential to categorize their associated slip histories (Faulkner et al., 2010). Inelastic deformation within the host rock is expected to form already before and during the early stages of fault formation and growth (Anderson, 1951; Scholz, 2002). Field observations (e.g., Kim et al., 2004; Crider and Peacock, 2004; Di Toro et al., 2005; Faulkner et al., 2010), models of quasi-static (e.g., Pollard and Segall, 1987) and dynamic rupturing (Ben-Zion and Shi, 2005; Johri et al., 2014) show that zones of inelastic deformation develop around propagating faults for both aseismic and seismic slips, but in different ways (e.g., Faulkner et al., 2010). In the aseismic case, inelastic deformation would develop on both sides of the fault (i.e., symmetrical deformation), and might be related to the regional strain field (Figure 1a.1; e.g. Peng and Johnson, 1972). Alternatively, the aseismic slip would lack a prominent fault-related deformation zone (Figure 1a.2). In the seismic case, inelastic deformation would form mainly on one side of the fault (i.e., asymmetrical deformation), with relation to changeable stress field due to fault directivity and strain perturbations (Figure 1b; Ben-Zion and Shi, 2005; Ma and Andrews, 2010; Johri et al.,

3

63 2014). The potential of distinguishing between seismic and aseismic slips by characterizing the

64 geometry and distribution of the deformation around faults was previously explored mainly by

65 the distribution of brittle deformation markers such as veins, joint sets or microcracks (Faulkner

66 et al., 2010), yet it is not always clear which marker best portrays the zone of inelastic

67 deformation.

68 In this study, we characterize the zone of inelastic deformation around faults using anisotropy of

69 magnetic susceptibility (AMS)-based magnetic fabric analysis, aiming to distinguish between

70 aseismic and seismic origins of the faults. The AMS analysis has commonly been used for

71 quantifying inelastic deformation in sedimentary rocks (Parés, 2015). The magnetic fabrics

72 reflect the preferred alignment of crystals and grain shapes within a rock sample and, as such,

73 provide a powerful tool to characterize intrinsic deformation on a grain scale (Borradaile and

74 Jackson, 2010; Weinberger et al., 2017). Various intra- and inter-crystalline deformation

75 mechanisms contribute to the AMS, such as grain boundary sliding, dislocation glide, twinning,

76 and kinking (Evans et al., 2003). These mechanisms produce irreversible deformation without

77 destruction of the lattice integrity, and thus, magnetic fabrics provide a sensitive tool to assess

78 inelastic deformation even prior to the development of macroscopic brittle deformation (e.g.,

79 Larrasoaña et al., 2011). Another chief advantage of the AMS analysis for petrofabric

80 characterization is the averaging out of large numbers of grains over the whole volume of the

81 sample (~10 cm^3).

82 Previous works showed that magnetic fabrics in fault zones may developed during slow

83 geological processes as well as short and fast events such as earthquakes (Levi et al., 2006, 2014;

84 Casas-Sainz et al., 2018; Marcén et al., 2019; Elhanati et al., 2020). To test the applicability of

85 AMS to diagnose aseismic and seismic slips, we compare the magnetic fabrics around faults of

4

86 two end-member origins: (1) faults of known aseismic slip that represent slow and shallow

87 crustal deformation (Figure 1a), and, (2) faults of proven seismic slip origin that represent

88 earthquake-driven fast crustal deformation (Figure 1b). Levi et al. (2014) and Elhanati et at.

89 (2020) show that magnetic fabrics near co-seismic normal faults within the seismically-active

90 Dead Sea Fault (DSF) system indicate fault-related magnetic fabrics, explained in terms of

91 dynamic rupturing. In this study, we characterize the magnetic fabrics near normal faults that

92 represent shallow crustal deformation of aseismic origin. The comparison of the magnetic fabrics

93 around these two end-member types of faults allows us to test the hypothesis that the zone of

94 inelastic deformation around aseismic and seismic faults is essentially different and can be

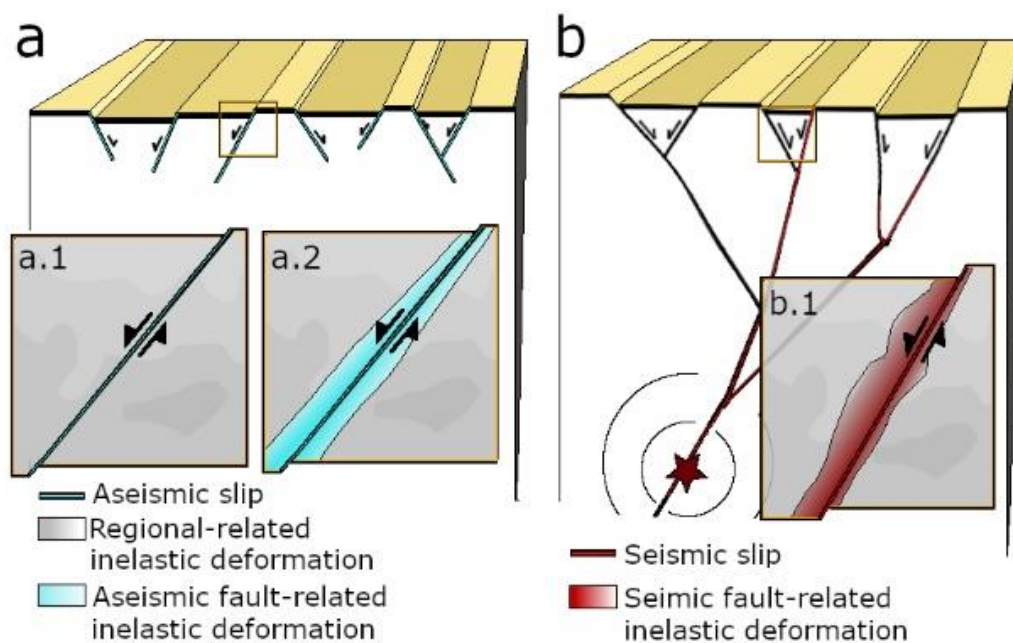95 distinguished by AMS analysis.

96

97 **Figure 1.** Structural setting of two end member types of faults and their associated inelastic
98 deformation: (a) Faults of aseismic origin represent shallow crustal deformation with regional strain-
99 related inelastic deformation (a.1), or fault-related inelastic deformation distributed symmetrically on
100 both sides of the fault (a.2). (b) Faults of seismic origin connected to a deep-seated hypocenter. The red

5

101 lines represent rupture propagation during a single event. Fault-related deformation is distributed
102 asymmetrically along one side of the fault.

103 **2. Magnetic Fabrics**

104 Magnetic fabrics describe the rock magnetic susceptibility tensor (**k**) with maximum,

105 intermediate, and minimum principal susceptibility axes - K_1, K_2, and K_3, respectively, which

106 correspond to $k_1 \geq k_2 \geq k_3$ eigenvalues (Rochette et al., 1992; and reference therein). Studies of the

107 magnetic fabrics of weakly deformed sedimentary rocks indicate that the orientation of the

108 principal susceptibility axes (AMS axes) are related and coaxial to the principal strain (or stress)

109 axes. Under sedimentary and compaction processes, K_3 axes align perpendicular to bedding and

110 K_2 and K_1 axes are scattered on a plane parallel to bedding (Type I, deposition and compaction;

111 Parés, 2015). In weakly tectonically deformed rocks, K_1 axes are often oriented along the

112 intersection of bedding and the tectonic flattening plane, whereas K_3 axes align perpendicular to

113 bedding (Type II, deformation). During slow progressive deformation, the magnetic fabrics often

114 show clusters of all three principal axes, and the K_1, K_2, and K_3 axes are coaxial with the

115 minimum (ε_3), intermediate (ε_2) and maximum (ε_1) shortening axes, respectively (Type III,

116 deformation; Borradaile and Jackson, 2010).

117 We use AMS data measured at room temperature (RT-AMS) as the main method for

118 characterizing the magnetic fabrics of the chalk sample. RT-AMS was measured at a low

119 magnetic field of 450 A/m and a frequency of 976 Hz with a KLY-4S Kappabridge (AGICO

120 Inc.) at the Geological Survey of Israel. To correlate the RT-AMS with specific minerals, we use

121 several experimental techniques, including measurements of AMS at low temperatures of ~77 K

122 (LT-AMS), anisotropy of anhysteretic remanence magnetization (AARM), vibrating sample

123 magnetometer (VSM) hysteresis loops, alternating field demagnetization curves (AF curves) and

6

124   temperature-dependent ($k_{(T)}$) susceptibility measurements. Experiments were performed at the

125   Geological Survey of Israel and at the Institute for Rock Magnetism, University of Minnesota.

126   The parameters used to characterize the magnetic fabrics, including the mean susceptibility

127   ($k_m=[k_1+k_2+k_3]/3$), degree of anisotropy ($P=k_1/k_3$), shape of anisotropy ($T=ln(F)$-

128     $ln(L)/ln(F)+ln(L)$), magnetic lineation ($L=k_1/k_2$) and magnetic foliation ($F=k_2/k_3$) were

129   calculated according to Jelinek (1981) using the Anisoft 4.2 software package (www.agico.com).

130   **3. Geologic Setting and Sampling**

131   We study two normal faults of aseismic origin within the Beer Sheva syncline. The syncline is an

132   approximately 100 km-long, ~35 km-wide that was formed during the Eocene under long-lasting

133   compressional regional stress field of NW maximum horizontal compression, denoted σH_{NW}

134   (Figure 2b) (Bahat, 1988; Levi et al., 2019). The Beer Sheva syncline is located within the Sinai

135   subplate and is spatially remote (60 km) from the active DSF system and any other known active

136   faults (Figure 2a) (Kurzon and Wetzler, 2019). Faults and joint sets were formed during burial in

137   the poorly consolidated pelagic chalk sediments at shallow depths (Buchbinder et al., 1988) and

138   represent paleostress regimes that are associated with the formation and uplift episodes of the

139   syncline (Bahat et al., 2005).

140   The studied faults (hereafter Fault A and Fault B) are exposed along the banks of Secher Creek

141   at the Beer Sheva syncline and are located ~120 m apart (Figure 2c). The faults cut chalks of the

142   middle Eocene Maresha Formation (Figure 2d) (Buchbinder et al., 1988). The ~10 m exposed

143   surfaces of the faults are accompanied by a few mm of fine-grained gouge layers. The faults

144   trend differently with an angle of 90° between their strikes: Fault A dips NW (52°/310°; dip/dip

145   direction) and is striking subparallel to the syncline axis; Fault B dips NE (41°/040°) and is

146   striking perpendicular to the syncline axis (Figure 2c and figure 3). The throw of both faults is

7

147   approximately 3.5 m. The faults are considered to form under wet conditions in the early burial

148   stages of the chalks during the formation of the Beer Sheva syncline (Buchbinder et al., 1988).

149   The studied chalks of the Maresha Formation have high porosity (>20%) (Palchik & Hatzor,

150   2002) and may contain up to 25% clay fraction (Nathan and Flexer, 1977). A previous AMS and

151   rock magnetic study of this formation demonstrates that the rocks contain pure diamagnetic

152   carbonate coccolith as the rocks matrix, paramagnetic clays (palygorskite and smectite), and

153   minor quantities of low-coercivity ferromagnetic Fe oxides (Issachar et al., 2018).

154   To construct the magnetic fabric profiles, we collected standard (25x25 mm) cylindrical core

155   samples along horizontal cross-sections, <0.2 m up to ~20 m from both sides of the tested faults

156   (Figure 2c). In addition, we sampled a reference outcrop, located ~50 m away from the faults

157   (Figure 2c). By this strategy, we provide a high-resolution "continuous" view of the inelastic

158   strain field around the faults. The sampling strategy allows us to diagnose three different

159   scenarios of magnetic fabrics: (1) regional-related fabrics, that are uniformly distributed on both

160   sides of the tested faults; (2) fault-related fabrics that are symmetrically distributed on both sides

161   of the fault with similar orientations of AMS axes within each block (i.e., unchangeable

162   distribution); and (3) fault-related fabrics that are developed asymmetrically mainly on one side

163   of the fault with varying orientations of AMS axes (i.e., changeable distribution).
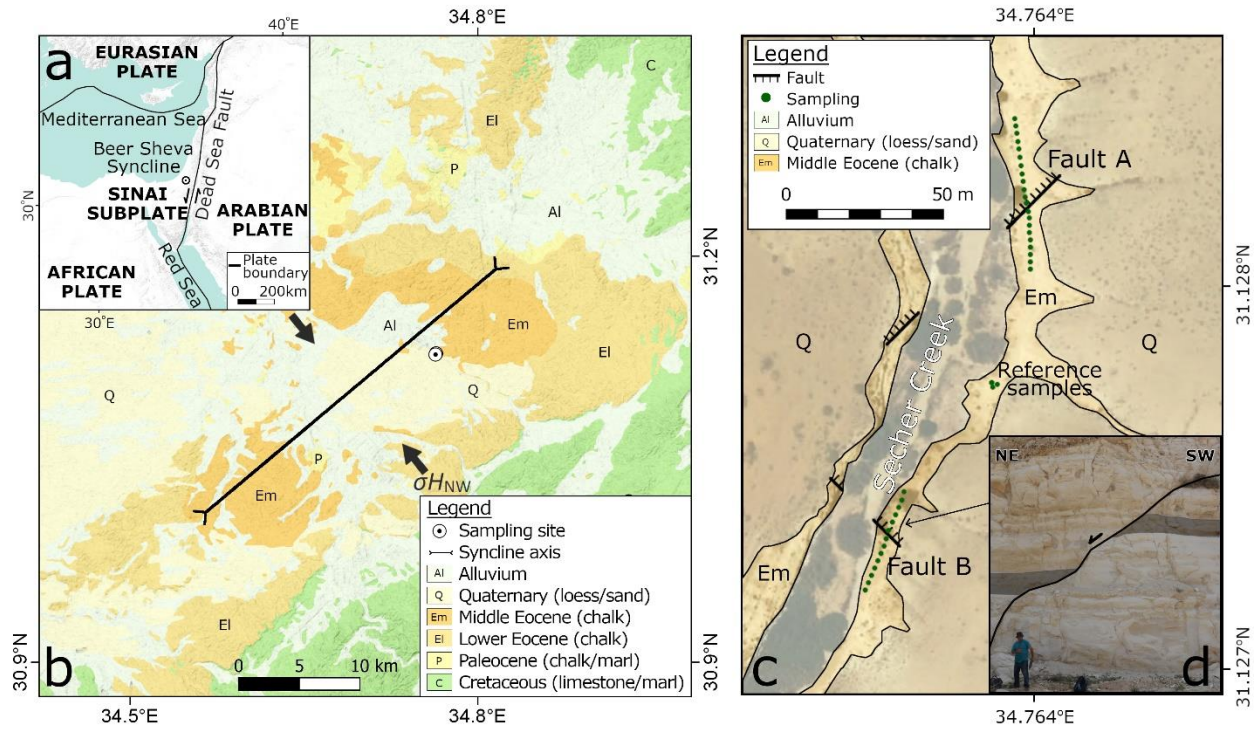
8

164

Figure 2. (a) General tectonic map of the study area. The circle marks the location of Beer Sheva syncline. (b) Geological map of the Beer Sheva syncline, showing Cretaceous to Quaternary strata (after Sneh et al., 1998), the syncline axis (after Bahat et al., 2005) and the direction of the regional stress field of σH_{NW}. (c) Detailed geological map of the study area, showing the fault traces cutting the middle Eocene strata and the distribution of the samples next to the faults (for more details see supporting information Table S1). (d) Photograph of Fault B showing an apparent fault dip and throw.

4. Results and Discussion

RT-AMS measurements of 111 chalk samples near the two tested faults indicate a narrow range of susceptibility values between 4 and 36 ($\times 10^{-6}$ SI) with a mean of 17 ± 7 ($\times 10^{-6}$ SI). The narrow range of the susceptibility values indicates that the samples has uniform mineralogy. The LT-AMS mean susceptibility value is 88 ± 21 ($\times 10^{-6}$ SI), indicating amplification factors of 4.6 ± 0.4 (supporting information Figure S1), and suggests that both paramagnetic and diamagnetic minerals contribute to the rocks susceptibility (Issachar et al., 2018). VSM hysteresis loops indicate positive linear response between -1 and 1 T. Yet, slope-corrected curves suggest minor

9

179 presence of low-coercivity ferromagnetic minerals. AF demagnetization curves indicate that

180 most of the remanent magnetization (up to 90%) is lost by a demagnetization field up to 60 mT,

181 suggesting that mostly low-coercivity minerals carry the remanent magnetization. Temperature-

182 dependent susceptibility curves indicate minor susceptibility changes during heating, suggesting

183 minor contribution of ferromagnetic minerals to the rocks susceptibility. Hence, we conclude that

184 the rocks predominantly contain diamagnetic carbonate minerals and paramagnetic clay minerals

185 with negligible presence of ferromagnetic minerals (supporting information Figure S2), in

186 accordance with previous magnetic fabrics of chalks from the area (Issachar et al., 2018).

187 LT-AMS and AARM fabrics show insignificant anisotropy and inconsistent orientations of

188 susceptibility axes, suggesting that neither paramagnetic nor ferromagnetic minerals are the

189 carriers of the RT-AMS (supporting information Figure S3 and Figure S4). The insignificant

190 anisotropies of the LT-AMS and AARM, the negligible ferromagnetic contribution and the

191 dominance of diamagnetic minerals (i.e., calcite) suggest that the RT-AMS is controlled by the

192 orientation distribution of the diamagnetic calcite minerals. Previous studies have shown that the

193 orientation of the AMS axes of calcite are sensitive strain indicators with K_3 axes parallel to the

194 compaction/shortening direction (e.g., Owens and Rutter, 1978; de Wall et al., 2000; Almqvist et

195 al., 2010; Issachar et al., 2018).

196 The orientation of the AMS axes of the studied chalk samples indicate deformation fabrics of

197 Type II, which is characterized by tight clusters of K_3 axes oriented sub-perpendicular to

198 bedding, and moderate to tight clusters of K_1 and K_2 axes within the bedding plane (Figure 3).

199 The AMS axes of samples collected from distance of <0.2 m up to 20 m from both sides of the

200 tested faults, as well as from the reference outcrop have similar and consistent orientations with

201 NE-SW trending K_1 axes and NW-SE trending K_2 axes (Figure 3). The K_1 and K_2 axes are

10

202 syncline parallel and syncline perpendicular, respectively, and are compatible with the syncline-

203 driven σH_{NW} stress field. Notably, irrespective to the attitude of the faults, the AMS axes around

204 them are similar and parallel to the syncline axes. In that sense, the AMS axes indicate uniform,

205 unchangeable distribution of inelastic deformation that is associated with the regional stress

206 field. The anisotropy P and shape T have values of 1.005 ± 0.003 and of 0.2 ± 0.4, respectively

207 (supporting information Figure S5 and Table S1). The AMS parameters show perceptible

208 differences between the blocks of the faults (supporting information Figure S5). The parameters

209 P and L have higher values in the footwall of Fault A and in the hanging wall of Fault B. The

210 shape of anisotropy is oblate ($T\sim1$) in the hanging wall of Fault A and is neutral ($T\sim0$) in its

211 footwall and in both blocks of Fault B. The F parameter shows no significant differences

212 between the blocks. The variations in the AMS parameters may imply that strain magnitudes

213 locally develop differently between the faulted blocks.

214 Fault observations and experiments show that inelastic deformation develops in association with

215 the regional stress field prior to host-rock faulting (e.g., Scholz, 1968; Mollema and Antonellini,

216 1999; Wilson et al., 2003; Crider and Peacock, 2004; Paterson and Wong, 2005; Blenkinsop,

217 2008). The faults of the current study are considered to form under wet conditions in the early

218 burial stages of the chalks (Buchbinder et al., 1988). The low strength of the chalks at the time of

219 the syncline formation could explain the absence of prominent fault-related deformation during

220 aseismic (i.e., creeping) slips on the faults. Hence, we suggest that the AMS axes represent the

221 regional stress (strain) field during the formation of the syncline and were already acquired prior

222 to the formation of the faults.

223 Contrary to the present findings, AMS studies of co-seismic faults within the active DSF system

224 infer prominent fault-related magnetic fabrics (Levi et al., 2014; Elhanati, 2019). Figure 4

11

225 presents the AMS results near two tested normal faults of a proven seismic origin (Marco et al.,

226 1996). The faults cut late Pleistocene soft sediments in the Masada Plain, Israel and are

227 associated with throw of ~2 m that occurred during single earthquake events (Marco and Agnon,

228 2005). The two tested faults were propagated throughout low-strength sediments, close to the

229 surface and under wet conditions (Marco et al., 1996). Several AMS characteristics are well

230 explained in terms of dynamic rupturing: (1) fault-related fabrics are asymmetrically distributed

231 between the fault blocks; (2) the orientation of AMS axes is changeable and occasionally

232 compatible with the principal strain directions defined by the fault focal-plane solutions; and (3)

233 the width of the deformation AMS fabric zone is roughly similar to the amount of displacement

234 during a single slip event. The faults in the Beer Sheva syncline and in the DSF system are

235 comparable as they have similar throw and were developed in low strength carbonate sediments

236 at shallow depth under wet conditions. The comparison of the magnetic fabrics of these two end-

237 member type of faults shows clearly that only the seismic faults form a prominent fault-related

238 magnetic fabrics (Figure 5a and Figure 5c). Nevertheless, we do not dispute the possible

239 formation of fault-related magnetic fabrics around aseismic faults that would differ from those

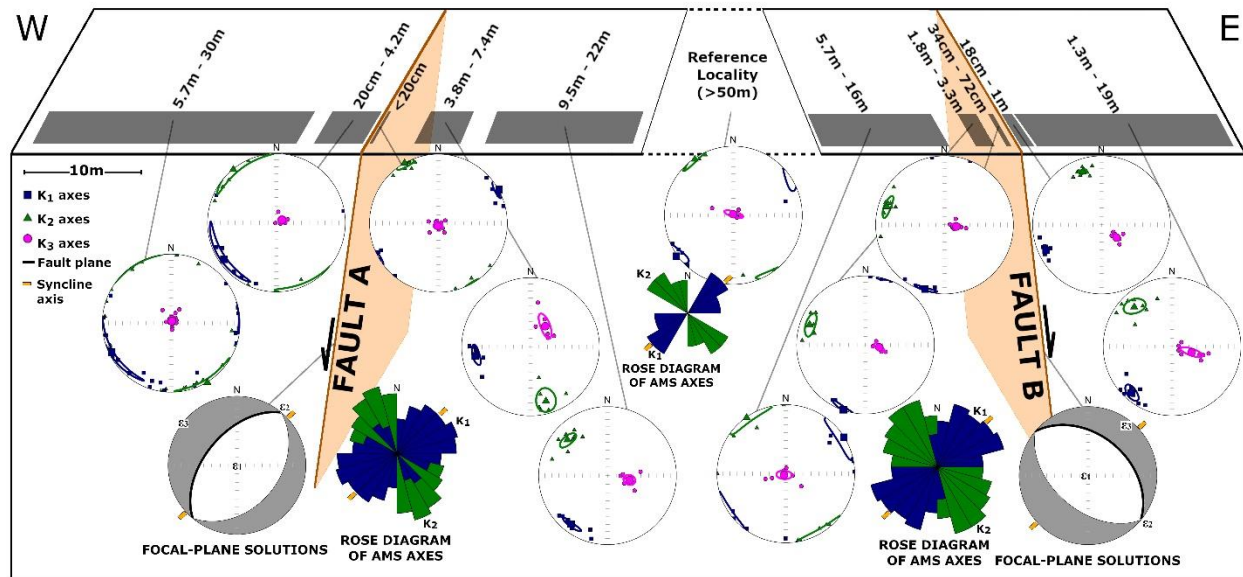240 around seismic faults (Figure 5b).

12

241

Figure 3. RT-AMS magnetic fabrics from sites at varied distances from aseismic faults (Fault A and Fault B) in the Beer Sheva syncline. Stereoplots are lower-hemisphere, equal-area projection of AMS principal axes, and the 95% confidence ellipses. The AMS axes show clustering of three principal axes indicating deformation origin. Rose diagrams show that the K_1 axes trend NE-SW parallel to the syncline axis (yellow line), and the K_2 axes trend NW-SE perpendicular to the syncline axis. Focal-plane solutions for the studied normal faults are indicated with ε, ε_2, and ε_3 are the infinitesimal maximum, intermediate and minimum principal strain axes, respectively.
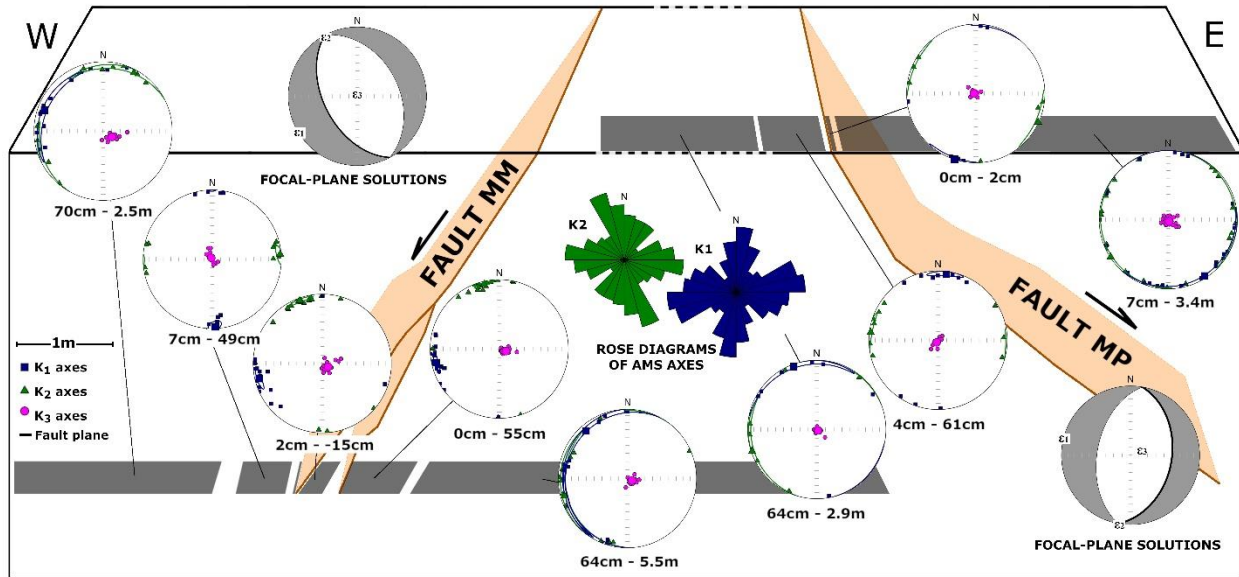
13

249

Figure 4. RT-AMS magnetic fabrics from sites at varied distances from co-seismic faults (Fault MM and Fault MP) in the Dead Sea Fault system, after Levi et al. (2014). The AMS axes show changeable orientations and asymmetrically distribution between the fault blocks. See Figure 3 for definition of steroplots and focal-plane solutions.
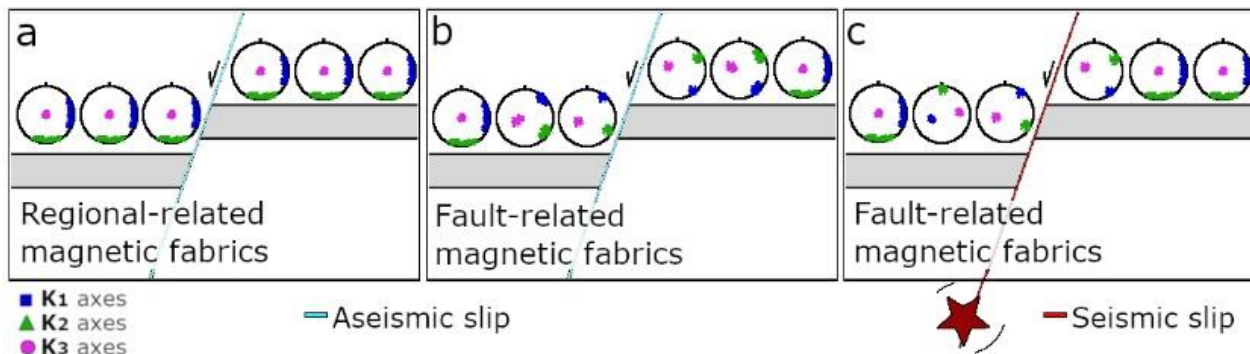

254

Figure 5. Conceptual model for AMS axes around faults. (a) Fault of aseismic origin showing AMS axes that are related only to the regional strain field. (b) Fault of aseismic origin with fault-related AMS axes on both sides of the fault, indicating an unchangeable strain field in each block. (c) Faults of seismic origin showing fault-related AMS axes mainly on one side of the fault, which indicate a changeable strain field. Note that away (>50 m) from the faults in (b) and (c), the magnetic fabrics could be of type I (deposition, compaction).

14

261   **5. Conclusions**

262   We measured the magnetic fabrics around two mesoscale faults of aseismic origin. The results

263   show robust and consistent magnetic fabrics of deformation origin, implying that AMS provides

264   a sensitive deformation marker to study inelastic deformation in the host rock. The orientation of

265   the AMS axes indicate symmetric and unchangeable magnetic fabrics of deformation origin on

266   both sides of the studied faults, showing a strong association with the syncline axis and the

267   regional strain field. The symmetrical and unchangeable regional-related magnetic fabrics are

268   compatible with observations and models of strain field around aseismic fault formation. The

269   present results were compared with previous magnetic fabric around co-seismic faults that also

270   formed in low strength sediments at shallow depths under wet conditions. Next to these fault, the

271   magnetic fabrics are changeable and asymmetrically distributed. In light of the current results

272   and previous aforementioned magnetic fabric studies, we suggest that magnetic fabric analysis

273   provides a powerful and sensitive tool to characterize inelastic deformation around faults. We

274   highlight the new possibility of using magnetic fabric analysis to distinguish between aseismic

275   and seismic slip histories.

279   The data used in this paper are available for download at:

280   https://figshare.com/s/c6331844fa5cdf0580c5.

281

282   **7. References**

283   Almqvist, B.S.G., Herwegh, M., Schmidt, V., Pettke, T., and Hirt, A.M., 2010, Magnetic

284   susceptibility as a tool to study deformed calcite with variable impurity content:

285   Geochemistry Geophysics Geosystems, v. 11, doi:Q01z0910.1029/2009gc002900.

286   Anderson, E.M., 1951, The dynamics of faulting and dyke formation with applications to Britain:

287   Oliver and Boyd.

288   Ault, A.K., 2020, Hematite fault rock thermochronometry and textures inform fault zone

289   processes: Journal of Structural Geology, v. 133, p. 104002, doi:10.1016/j.jsg.2020.104002.

290   Bahat, D., 1988, Early single-layer and late multi-layer joints in the Lower Eocene chalks near

291   Beer Sheva, Israel: Annales Tectonicae II, p. 3–11.

292   Bahat, D., Rabinovitch, A., and Frid, V., 2005, Tensile Fracturing in Rocks: Heidelberg,

293   Springer, 251–279 p., doi:2004108439.

294   Ben-Zion, Y., and Shi, Z., 2005, Dynamic rupture on a material interface with spontaneous

295   generation of plastic strain in the bulk: Earth and Planetary Science Letters, v. 236, p. 486–

296   496, doi:10.1016/J.EPSL.2005.03.025.

297   Blenkinsop, T.G., 2008, Relationships between faults, extension fractures and veins, and stress:

298   Journal of Structural Geology, v. 30, p. 622–632, doi:10.1016/J.JSG.2008.01.008.

299   Borradaile, G.J., and Jackson, M., 2010, Structural geology, petrofabrics and magnetic fabrics

300   (AMS, AARM, AIRM): Journal of Structural Geology, v. 32, p. 1519–1551,

301   doi:10.1016/j.jsg.2009.09.006.

302   Buchbinder, B., Benjamini, C., Mimran, Y., and Gvirtzman, G., 1988, Mass transport in Eocene

303   pelagic chalk on the northwestern edge of the Arabian platform, Shefela area, Israel:

16

304   Sedimentology, v. 35, p. 257–274, doi:10.1111/j.1365-3091.1988.tb00948.x.

305   Casas-Sainz, A.M. et al., 2018, Strain indicators and magnetic fabric in intraplate fault zones:

306   Case study of Daroca thrust, Iberian Chain, Spain: Tectonophysics, v. 730, p. 29–47,

307   doi:10.1016/J.TECTO.2018.02.013.

308   Crider, J.G., and Peacock, D.C., 2004, Initiation of brittle faults in the upper crust: a review of

309   field   observations: Journal   of   Structural   Geology,   v.   26,   p.   691–707,

310   doi:10.1016/J.JSG.2003.07.007.

311   Elhanati, D., 2019, Characterizing the strain field around co-seismic faults using magnetic

312   fabrics (MSc Thesis): Tel Aviv University.

313   Elhanati, D., Levi, T., Marco, S., and Weinberger, R., 2020, Zones of inelastic deformation

314   around surface ruptures detected by magnetic fabrics: Tectonophysics, v. 788, p. 228502,

315   doi:10.1016/j.tecto.2020.228502.

316   Evans, M.A., Lewchuk, M.T., and Elmore, R.D., 2003, Strain partitioning of deformation

317   mechanisms in limestones: examining the relationship of strain and anisotropy of magnetic

318   susceptibility   (AMS):   Journal   of   Structural   Geology,   v.   25,   p.   1525–1549,

319   doi:10.1016/S0191-8141(02)00186-4.

320   Faulkner, D.R., Jackson, C.A.L., Lunn, R.J., Schlische, R.W., Shipton, Z.K., Wibberley, C.A.J.,

321   and Withjack, M.O., 2010, A review of recent developments concerning the structure,

322   mechanics and fluid flow properties of fault zones: Journal of Structural Geology, v. 32, p.

323   1557–1575, doi:10.1016/J.JSG.2010.06.009.

324   Issachar, R., Levi, T., Marco, S., and Weinberger, R., 2018, Separation of Diamagnetic and

325   Paramagnetic Fabrics Reveals Strain Directions in Carbonate Rocks: Journal of

17

326   Geophysical Research: Solid Earth, v. 123, p. 2035–2048, doi:10.1002/2017JB014823.

327   Jelinek, V., 1981, Characterization of the magnetic fabric of rocks: Tectonophysics, v. 79, p.

328   T63–T67, doi:10.1016/0040-1951(81)90110-4.

329   Johri, M., Dunham, E.M., Zoback, M.D., and Fang, Z., 2014, Predicting fault damage zones by

330   modeling dynamic rupture propagation and comparison with field observations: Journal of

331   Geophysical Research: Solid Earth, v. 119, p. 1251–1272, doi:10.1002/2013JB010335.

332   Kim, Y.-S., Peacock, D.C.., and Sanderson, D.J., 2004, Fault damage zones: Journal of

333   Structural Geology, v. 26, p. 503–517, doi:10.1016/J.JSG.2003.08.002.

334   Kurzon, I., and Wetzler, N., 2019, Defining and mapping capable tectonic sources for seismic

335   hazard estimation in Israel: general analysis and specific focus for nuclear power plants in

336   Israel. Report GSI/21/15. Geological Survey of Israel (2015).:

337   Larrasoaña, J.C., Gómez-Paccard, M., Giralt, S., and Roberts, A.P., 2011, Rapid locking of

338   tectonic magnetic fabrics in weakly deformed mudrocks: Tectonophysics, v. 507, p. 16–25,

339   doi:10.1016/j.tecto.2011.05.003.

340   Levi, T., Avni, Y., and Bahat, D., 2019, Evolution of the stress field near the Arava basin located

341   along the Dead Sea Fault system as revealed by joint sets: Journal of Structural Geology, v.

342   128, p. 103876, doi:10.1016/J.JSG.2019.103876.

343   Levi, T., Weinberger, R., Aïfa, T., Eyal, Y., and Marco, S., 2006, Injection mechanism of clay-

344   rich sediments into dikes during earthquakes: Geochemistry, Geophysics, and Geosystems,

345   v. 7, p. Q12009 (doi:10.1029/2006GC001410).

346   Levi, T., Weinberger, R., and Marco, S., 2014, Magnetic fabrics induced by dynamic faulting

347   reveal damage zone sizes in soft rocks, Dead Sea basin: Geophysical Journal International,

18

348   v. 199, p. 1214–1229, doi:10.1093/gji/ggu300.

349   Ma, S., and Andrews, D.J., 2010, Inelastic off-fault response and three-dimensional dynamics of

350   earthquake rupture on a strike-slip fault: Journal of Geophysical Research, v. 115, p.

351   B04304, doi:10.1029/2009JB006382.

352   Marcén, M., Román-Berdiel, T., Casas-Sainz, A.M., Soto, R., Oliva-Urcia, B., and Castro, J.,

353   2019, Strain variations in a seismogenic normal fault (Baza Sub-basin, Betic Chain):

354   Insights from magnetic fabrics (AMS): Tectonophysics, v. 765, p. 64–82,

355   doi:10.1016/J.TECTO.2019.05.014.

356   Marco, S., and Agnon, A., 2005, High-resolution stratigraphy reveals repeated earthquake

357   faulting in the Masada Fault Zone, Dead Sea Transform: Tectonophysics, v. 408, p. 101–

358   112.

359   Marco, S., Stein, M., Agnon, A., and Ron, H., 1996, Long term earthquake clustering: a 50,000

360   year paleoseismic record in the Dead Sea Graben: J. Geophys. Res., v. 101, p. 6179–6192.

361   Mollema, P.N., and Antonellini, M., 1999, Development of strike-slip faults in the dolomites of

362   the Sella Group, Northern Italy: Journal of Structural Geology, v. 21, p. 273–292,

363   doi:10.1016/S0191-8141(98)00121-7.

364   Nathan, Y., and Flexer, A., 1977, Clinoptilolite, paragenesis and stratigraphy: Sedimentology,

365   http://onlinelibrary.wiley.com/doi/10.1111/j.1365-3091.1977.tb01919.x/abstract (accessed

366   September 2015).

367   Owens, W.H., and Rutter, E.H., 1978, The development of magnetic susceptibility anisotropy

368   through crystallographic preferred orientation in a calcite rock: Physics of the Earth and

369   Planetary Interiors, v. 16, p. 215–222,

19

370   http://www.sciencedirect.com/science/article/pii/0031920178900146.

371   Parés, J.M., 2015, Sixty years of anisotropy of magnetic susceptibility in deformed sedimentary

372   rocks: Frontiers in Earth Science, v. 3, doi:10.3389/feart.2015.00004.

373   Paterson, M.S., and Wong, T.F., 2005, Experimental rock deformation-the brittle field: Springer

374   Science & Business Media.

375   Peng, S., and Johnson, A.M., 1972, Crack growth and faulting in cylindrical specimens of

376   chelmsford granite: International Journal of Rock Mechanics and Mining Sciences and, v. 9,

377   p. 37–86, doi:10.1016/0148-9062(72)90050-2.

378   Pollard, D.D., and Segall, P., 1987, Theoretical displacements and stresses near fractures in rock:

379   with applications to faults, joints, veins, dikes, and solution surfacese, *in* In Fracture

380   mechanics of rock, p. 277–347.

381   Rochette, P., Jackson, M., and Aubourg, C., 1992, Rock magnetism and the interpretation of

382   anisotropy of magnetic susceptibility: Reviews of Geophysics, v. 30, p. 209,

383   doi:10.1029/92RG00733.

384   Rowe, C.D., and Griffith, W.A., 2015, Do faults preserve a record of seismic slip: A second

385   opinion: Journal of Structural Geology, v. 78, p. 1–26, doi:10.1016/J.JSG.2015.06.006.

386   Scholz, C.H., 1968, Microfracturing and the inelastic deformation of rock in compression:

387   Journal of Geophysical Research, v. 73, p. 1417–1432, doi:10.1029/JB073i004p01417.

388   Scholz, C.H., 2002, The Mechanics of Earthquakes and Faulting: New York, Cambridge Univ.

389   Press, 439 p.

390   Di Toro, G., Nielsen, S., and Pennacchioni, G., 2005, Earthquake rupture dynamics frozen in

391   exhumed ancient faults: Nature, v. 436, p. 1009–1012, doi:10.1038/nature03910.

20

392   de Wall, H., Bestmann, M., and Ullemeyer, K., 2000, Anisotropy of diamagnetic susceptibility in

393   Thassos marble: A comparison between measured and modeled data: Journal of Structural

394   Geology, v. 22, p. 1761–1771, doi:10.1016/s0191-8141(00)00105-x.

395   Weinberger, R., Levi, T., Alsop, G.I., and Marco, S., 2017, Kinematics of Mass Transport

396   Deposits revealed by magnetic fabrics: Geophysical Research Letters, v. 44, p. 7743–7749,

397   doi:10.1002/2017GL074471.

398   Wilson, J.., Chester, J.., and Chester, F.., 2003, Microfracture analysis of fault growth and wear

399   processes, Punchbowl Fault, San Andreas system, California: Journal of Structural Geology,

400   v. 25, p. 1855–1873, doi:10.1016/S0191-8141(03)00036-1.

401